# Energy Minimization Algorithms for Image-Guided Automatic Patch Clamp Systems

Summary of the Ph.D. thesis

**Krisztián Koós**
BIOMAG group
Biological Research Centre, Szeged

Supervisor:
Dr. Peter Horvath


Doctoral School of Computer Science
Faculty of Science and Informatics
University of Szeged
Szeged, 2019

# Introduction

Image analysis algorithms and tools have pushed the frontiers of scientific computing in the last few decades. Biological imaging is one of the fields where the modern computer has made a remarkable impact. Advanced microscopes can now easily collect thousands of high-resolution images of cells daily. It was soon realized that automation is beneficial to extract the full spectrum of information present in these images.

Brightfield microscopy is a simple optical microscopy technique where visible light is transmitted through the sample and a system of lenses magnifies images of small objects. Contrast enhancing techniques, for example, differential interference contrast (DIC) microscopy, are able to show features that are invisible otherwise. Such label-free techniques allow the study of the internal structure of living cells.

The scientific recognition that electrical phenomena are part of animal physiology is well known by now. The electrophysiology of brain cells is investigated by the patch clamp technique. This helps in understanding the complex structure of the brain and discovering new cellular phenotypes. The technique is very laborious and requires expertise, but can be automated. The dissertation details the algorithms we have developed for a software system that fully automatically performs patch clamp recordings on brain tissue slices using label-free microscopy. The results are grouped into three major thesis points which are summarized below. The relation between these thesis points and their supporting publications is shown in Table 1.

| **Part** | [1] | [2] | [3] | [4] | [5] | [6] | [7] |
|---|---|---|---|---|---|---|---|
| I. | • | • | • | | | | |
| II. | | | | • | • | | |
| III. | | | | | • | • | • |

Table 1. Thesis contributions and supporting publications.

# Part I: DIC Image Processing

DIC images – and label-free images in general – are easy to understand for the human eye but conventional algorithms are not applicable when it comes to image processing. The characteristic of these images is their shadow-cast appearance which makes them deceptively three-dimensional. Mathematically, they are similar to gradient images.

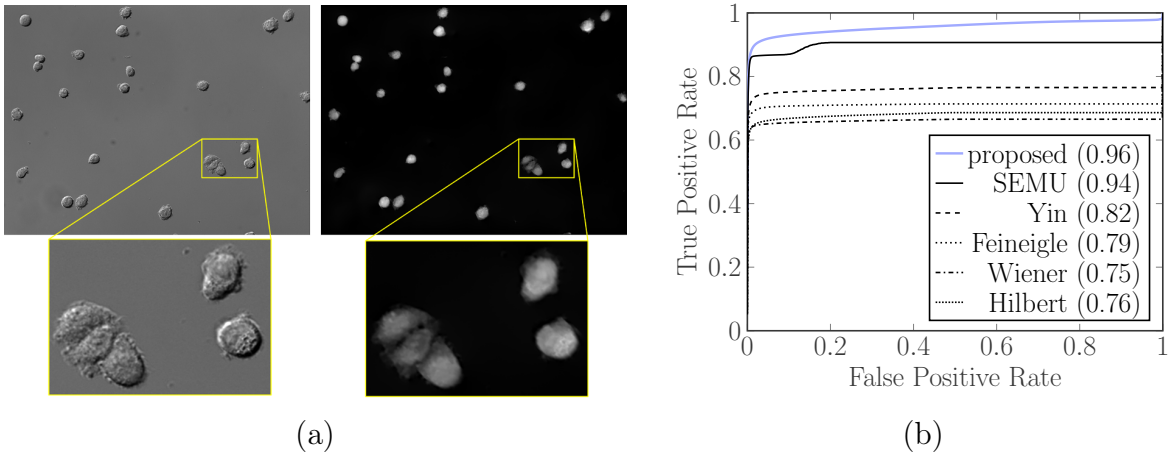


(a) (b)

Figure 1. Comparison of algorithms on cell images. (a) Example DIC image of CHO cells and its reconstruction with the proposed algorithm. (b) Average ROC Curves on cell images. The numbers in the legend show the AUC values.

We have developed algorithms and tools to make DIC image analysis easier and more reliable.

We have developed a differential geometry based reconstruction algorithm which transforms the images similar to fluorescence ones to make analysis easier. The method incorporates the point spread function (PSF) of the microscope which leads to better reconstructions. Mathematically this is described by a double integral in the energy function written as:

$$E = \frac{1}{2} \iint\limits_{\Omega} \left[ \mathbf{u} \cdot \nabla \hat{I} - (G - c) \right]^2 d\Omega + \lambda \iint\limits_{\Omega} |\nabla I| \, d\Omega, \tag{1}$$

where $\Omega$ is the domain, the shear angle $\mathbf{u}$ is a two-element unit vector, $I$ is the object information in question, $G$ is the input image, and $c$ is an arbitrary constant. Calculating its Euler-Lagrangian functions is challenging. However, if we use a correct approximation of the point spread function as the kernel function, the perturbation function of the data term can be replaced with its Taylor series. This function is convergent around each image point at least in the domain of the local integral. The state of the art quality of the algorithm is demonstrated on three different datasets which we generated. One dataset consists of simulated images. The other two are real images of miniaturized objects with fluorescence ground truth and cell images with hand-segmentations. Fig. 1 shows an example image of cells and its reconstruction, and the comparison of the examined algorithms on the cell dataset.

The transformed images directly contain morphological information of the sample but their extension in the Z dimension is unclear. We have proposed an algorithm for

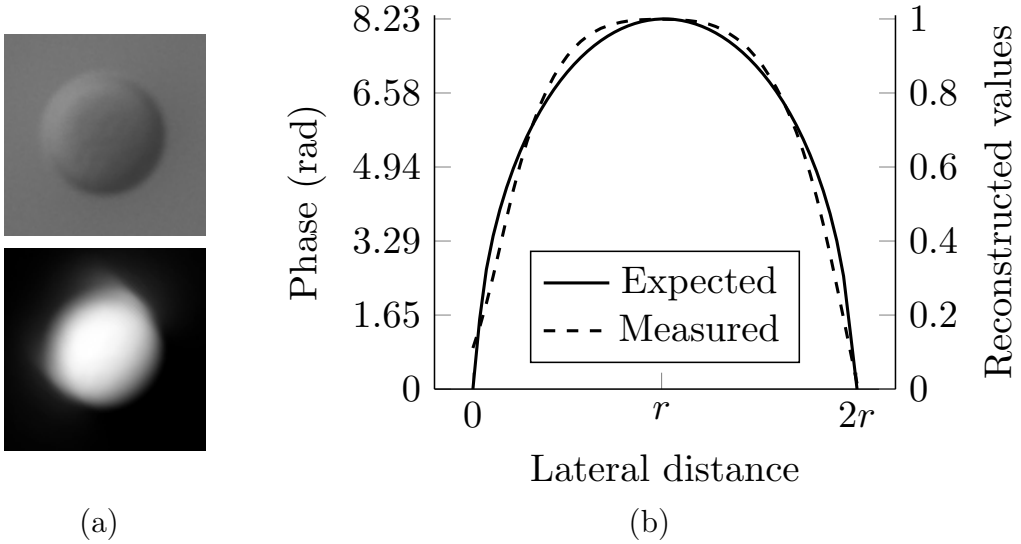


Figure 2. Phase calibration on microbeads. (a) Example DIC image of a microbead and its reconstruction. (b) Line profile of the phase distribution of microbeads

phase and height measurement using DIC microscopy. This calibration step is performed by taking images of microbeads with a known refractive index and calculating a function that maps the pixel intensities to physical properties. Fig. 2 summarizes the process. Part b of the figure contains both the theoretical and the measured line profiles. The radius of the bead is denoted by $r$. The measured values originate from 16 beads, averaged after normalization and from 4 directions (horizontal, vertical and two diagonals) through their centers. The technique provides a simple and cost-effective solution to phase measurement without the need of additional microscope parts, and it performs reliably using just a single image.

The author's main contributions to this work are the following:

- Design of the energy function based on the mathematical description of the microscope's image formation model.
- Implementation of the developed and examined algorithms.
- Design and generation of synthetic tests. Design of further tests and imaging of the samples. Evaluation of the algorithms on the datasets.
- Elaboration and evaluation of the algorithm for phase measurement.

# Part II: Patch Clamp Pipette Detection Models

Segmentation of objects with well-defined geometries is a fundamental problem in image analysis. Several methods were proposed to detect lines, ellipses or rectangles to identify roads, trees, or houses, respectively, using marked point processes (MPP). Another way is to compromise strict geometries and use variational methods. For example higher-order active contours (HOAC) that can describe various objects with defined shape allowing slight variations of the boundaries. HOACs were successfully used to model circular objects or complex road structures. Recently a family of hybrid variational models was proposed that is capable of capturing circular and elliptical objects by minimizing only a few parameters. We have presented a variational method that extends the latter model and detects elongated straight object pairs that have a common reference point. We use this model to segment pipette tips under a microscope and automatically navigate these tips with micrometer precision for patch clamping and measuring properties of nerve cells.

Three variants of the proposed Pipette Hunter tip detection model are presented which are all variational frameworks. The methods work on differential interference contrast, oblique (Hoffman modulation contrast), and fluorescence microscopy image stacks that contain optically sliced images of a pipette. The inputs are either different projections of the image stack or the stack itself, depending on the number of dimensions supported by the algorithm.

The 2D method fits two rectangles to the image. The main idea is to cover dark image regions (the edges of the pipette) with two long rectangles given some constraints. The rectangles are aligned with two line segments that have a common end point, also called a pivot point. The pivot point is the reference point of the two

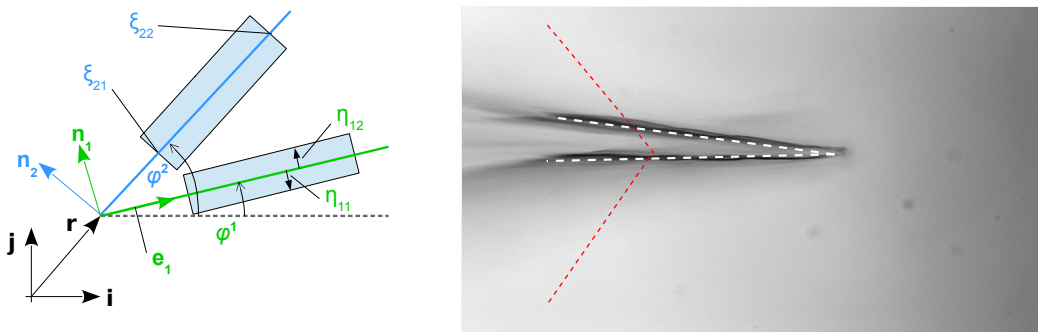


(a) (b)

Figure 3. The 2D Pipette Hunter model. (a) The configuration of the model. (b) The result of the detection.

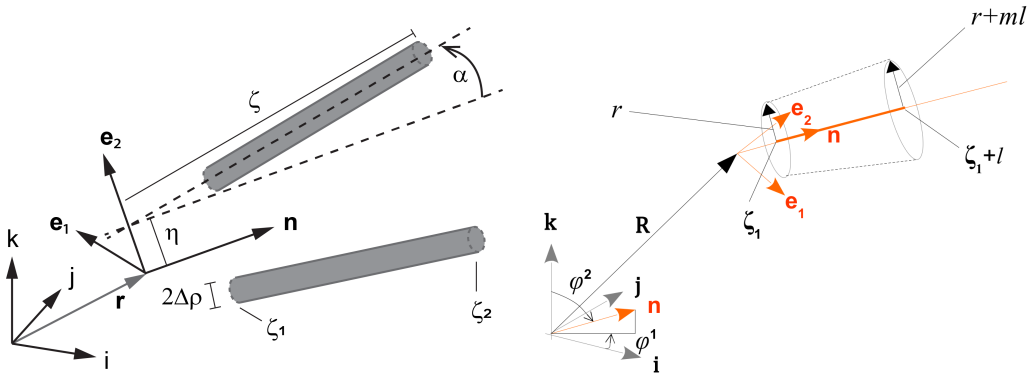


Figure 4. 3D pipette detection models. Configuration (a) for label-free images and (b) for fluorescence images.

rectangles. The line segments are called legs. The energy function of this configuration is the sum of the energies of the individual legs:

$$E_{2D} = \sum_{i=1}^{2} \frac{1}{A} \int_{\eta_i=\eta_{i1}}^{\eta_{i2}} \int_{\xi_i=\xi_{i1}}^{\xi_{i2}} I\left(\mathbf{p}_i\right) \, d\xi_i \, d\eta_i. \tag{2}$$

The points $\mathbf{p}_i$ are the pixel positions covered by the model and are detailed in the dissertation. Fig. 3 shows the configuration and a result in an example image. The pivot point is given by its position vector $\mathbf{r} = x^1\mathbf{i} + x^2\mathbf{j}$. The rotation of the legs around the pivot point is given by the $\varphi^1$ and $\varphi^2$ variables. Red lines are the starting position of the legs, white lines are the state of the legs after the algorithm terminated.

The first 3D method which works on label-free images fits two cylinders that also have a pivot point. It takes an image stack of the pipette as input and results in a 3D point in one pass. Since 3D algorithms usually have many degrees of freedom (DOF) it is reasonable to apply some initialization algorithm to determine the starting point instead of a swarm start. We developed an initialization algorithm which is based on a moving line profile in the image and looks for a strong intensity drop. The energy function of this configuration, similarly to the 2D model, is the integral of the voxel intensities covered by the two legs:

$$E_{3Dlf} = \int_V \left[I\left(\mathbf{P}_+\right) + I\left(\mathbf{P}_-\right)\right] dV = \int_{\zeta_1}^{\zeta_2} \int_0^{2\pi} \int_0^{\triangle\rho} \left[I\left(\mathbf{P}_+\right) + I\left(\mathbf{P}_-\right)\right] \rho \, d\rho \, d\phi \, d\zeta, \tag{3}$$

where $\mathbf{P}$ are the internal points of the cylinders and $V$ is the volume of the mechanism. Fig. 4a illustrates the setup of this model. $\eta$ is a distance and $\alpha$ is a rotation given relative to two different axes of the moving local frame.

| Algorithm | Std. error (µm) | Std. dev. (µm) | Std. error (pixel/voxel) | Std. dev. (pixel/voxel) |
|---|---|---|---|---|
| 2D Pipette Hunter | 3.53 | 2.47 | 32.97 | 23.10 |
| 3D label-free | 0.99 | 0.55 | 8.63 | 4.80 |
| 3D fluorescence | N/A | N/A | 75.66 | 30.97 |

Table 2. Accuracies of the pipette detection algorithms.

The second 3D model also takes an image stack of a pipette as input which is acquired using fluorescence imaging. In this case, the pipette has to be filled with fluorescent material which is not possible in some biological applications. The algorithm tries to fit a (truncated) cone as illustrated in Fig. 4b. Although the DOF is 8 in both 3D models (the third rotation angle $\varphi^3$ is constrained due to symmetry), their meanings differ. For example, in the fluorescent case the height of the cone or the radius of the base(s) can change while these are fixed in the case of the label-free model. The normalized energy function is described as follows:

$$E_{3Df} = \frac{1}{V} \int_V I\left(\mathbf{P}\right) \, dV = \frac{1}{V} \int_{\phi=0}^{2\pi} \int_{\zeta=\zeta_1}^{\zeta_1+l} \int_{\rho=0}^{r+m(\zeta-\zeta_1)} I\left(\mathbf{P}\right) \rho \, d\rho \, d\zeta \, d\phi. \tag{4}$$

The quality of the algorithms is measured by comparing the results to hand-picked ground truth tip positions, summarized in Table 2. The accuracies of the detections are high enough to reliably hit target cells. The algorithms are implemented in our patch clamp system using vectorized code to keep the runtime low despite its gradient descent nature. We believe our method can be used in other applications, e.g. road intersection detection or neural circuit segmentation.

The author's main contributions to this work are the following:

- Design of the energy function.
- Parallelized implementation of the algorithms.
- Dataset generation and algorithm evaluation.

# Part III: Automated Microscopy and Applications

Recently, the automation of patch clamp technique has emerged to image guided systems. We have developed the first fully automated label-free patch clamp system enabling the study of human samples. The system is controlled by a single software, including all hardware components, data handling, and visualization. For the patch clamping procedure it uses single-cell approaching strategies, such as micrometer precision calibration, registration, and navigation of the pipette tip, elastic real-time 3D tracking of the target cell, bypassing obstacles e.g. cells or other tissue components while the tip approaches its target at a few micrometer precision, and an advanced pressure controller system that substitutes the classical manual pressure protocols throughout the process. A central part of the method was the detection of single neurons in label-free 3D images by generating a new image database and training a deep convolutional neural network.

The steps of the developed visual patch clamp recording process are illustrated in Fig. 5. In order to use the system for the first time, a pipette calibration step has to be performed to allow for the pipette to be moved relatively to the camera's plane (1). Thereafter, a position update is made after every pipette change (2) using the built-in pipette detection algorithms described in Chapter 4 of the dissertation to overcome the problem caused by length differences of pipettes (3). At this point, the system is ready to select a target and approach it to perform recordings. We have acquired and annotated a single cell database of brain tissue images, to our knowledge the largest 3D set of this kind. A convolutional deep neural network was trained on this dataset for cell detection. The system can automatically select a cell for recording (4). When a cell is selected, multiple subsystems are started parallelly that perform the patch clamp process:

i) A subsystem adjusts the electrode and slowly pushes it forward next to the cell. If any obstacle is found in the way, an avoidance algorithm tries to dodge it (5).

ii) A cell tracking system follows the possible shift of the cell (6) and adjusts the pipette's trajectory if necessary.

iii) During the whole process, a pressure regulator system assures that the requested pressure is available (7).

Once the pipette touches the cell (cell-attached configuration) the system performs gigaseal formation (8), breaks in the cell membrane (9) and then automatically starts the electrophysiology measurements (10).

At the end of the measurements, the implemented pipette cleaning method can

be performed or the next patch clamp recording can be started from the pipette tip position update step. An event logging system collects information during the patch clamp process, including the target locations and the outcome success, and report files can be generated at the end. We used the system for harvesting cytoplasm and nuclei from the recorded cells (11) and performed anatomical reconstruction on the samples (12).

After comparing the available machine learning tools we have decided to use deep learning for cell detection. Our software provides a labeling tool for dataset annotation. Field experts labeled 6344 cells on 265 stacks which took about 132 hours. The annotation procedure consisted of putting bounding boxes around the recognized cells over multiple slices in the stack. We used *caffe* inside Nvidia's DIGITS framework to train DetectNet with ADAM solver. The training run for 2500 epochs which took 6 days and 15 hours on a Titan Xp graphics card. The evaluation of the training resulted in 0.835 F1-score with 81.72% precision and 85.39% recall. The training and detection pipeline is depicted in Fig. 6. The prediction is not performed on the microscope's PC but on a dedicated GPU server using client-server communication. The detection time for a single image, including the time of data transfer between the computers is about 100 ms which is nearly real-time.

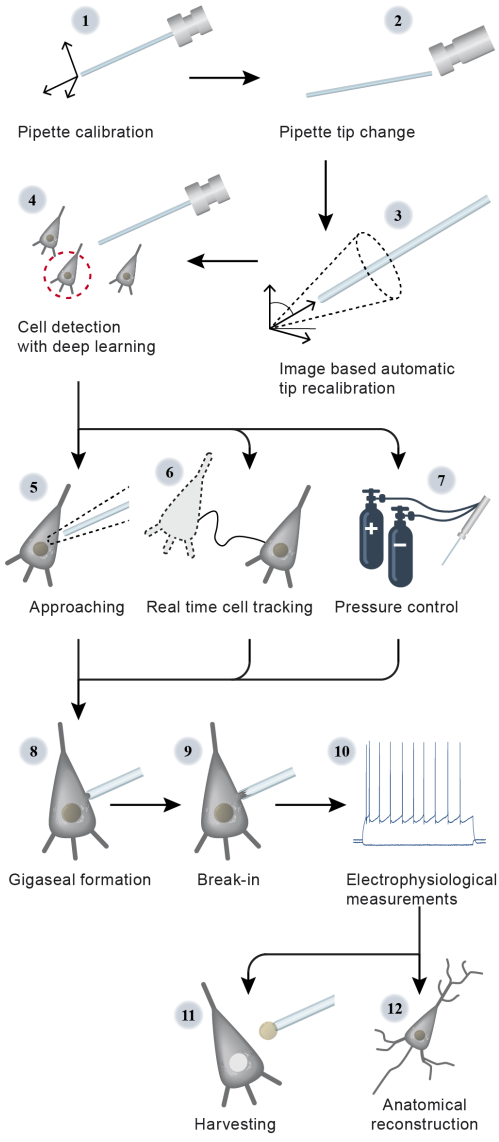


Figure 5. Steps of visual autopatching.

The target cell can be shifted during the patch clamping process while the pipette is pushed towards it. The shift can occur in any direction in the tissue and based on our experiments it is usually between 3 and 10 µm. Tracking the cell under the microscope is a challenging task because a 3-dimensional tracking is required with

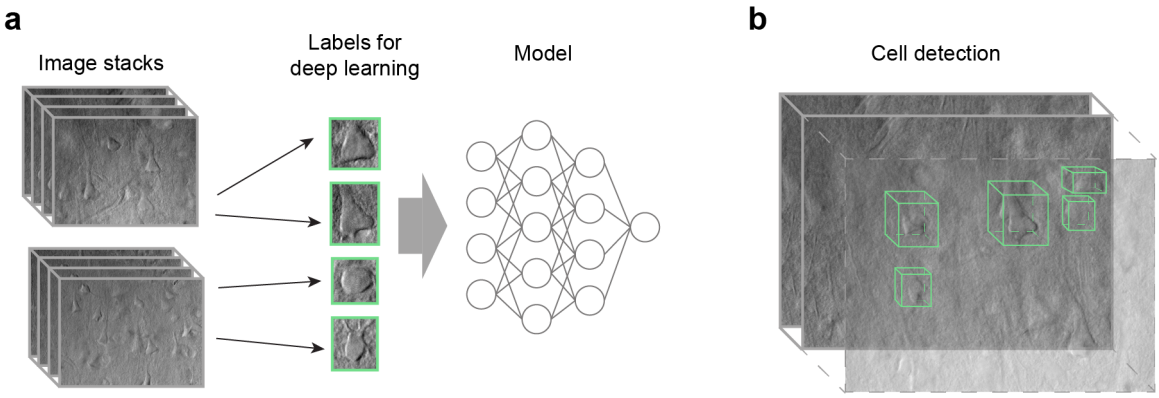


Figure 6. Cell detection in label-free tissues using deep learning. (a) Dataset generation and training. (b) Cell detection in unstained living neocortical tissues.

a 2-dimensional label-free modality. The developed online tracking system has two parts which run in separate phases. One part performs lateral tracking in the XY plane while the other part tracks the cell in the Z dimension. Both parts require a template image of the target cell which is acquired before starting the patch clamp process and when the cell is in focus in the image. The Kanade-Lucas-Tomasi (KLT) feature tracking algorithm is used as a lateral tracker with minimum eigenvalue feature points. This tracking is always performed in the image corresponding to the latest focus level. The Z tracking algorithm operates on a small image stack and it is based on general focus detection algorithms that try to optimize the image gradient. Acquiring an image stack is time-consuming as the objective has to be moved physically to different focus levels. Therefore, when Z tracking is being performed the pipette is not moved to ensure that the cell is not pushed away meanwhile. Fig. 7 shows an image of a target cell when the tracking started, ended, and finally the drift from the cell's original location by the arrows.

The control software manages all the hardware elements and algorithms. When

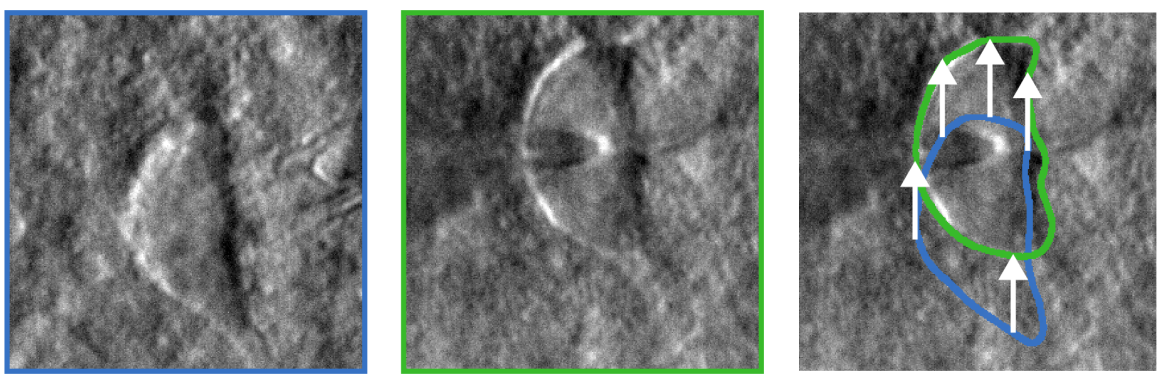

Figure 7. Cell tracking example.

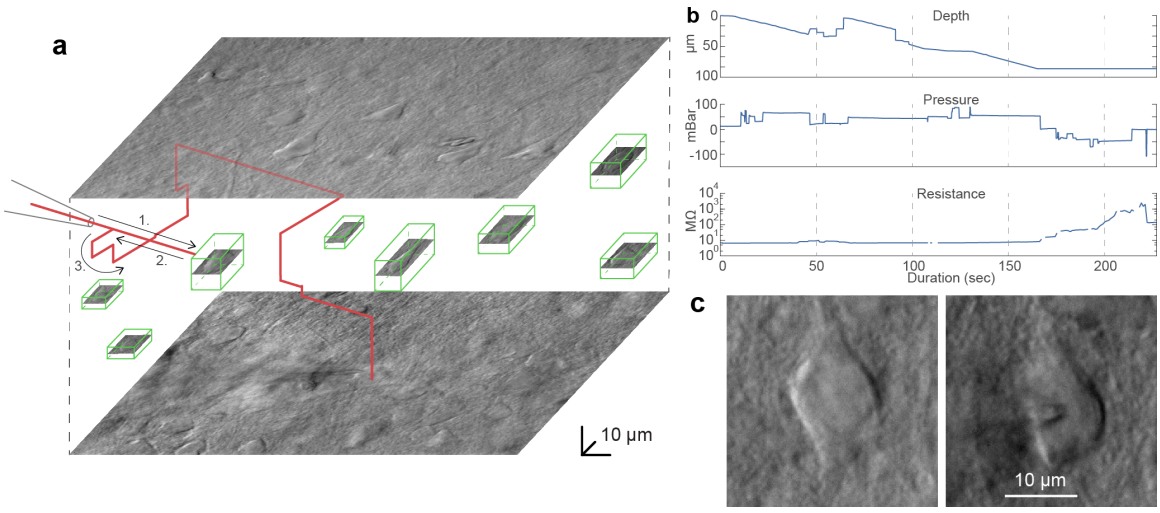


Figure 8. Representative example of a whole-cell recording. (a) Trajectory of the pipette tip in the tissue and the distribution of the detected cells. (b) Plots of the depth of the pipette tip in the tissue, the applied air pressure, and the measured series resistance during the approach. (c) Image of a cell before and after performing patch clamp recording on it.

initiating a patch clamp procedure, the pipette should already be calibrated and a target cell should be selected. Then the software calculates the trajectory of the pipette movement on which the manipulator moves the pipette tip close to the cell, and applies medium air pressure to the pipette. The initial trajectory is a straight line on the manipulators X-axis thus the distortion made in the tissue is minimal. Note that the X-axis of the manipulator is tilted against the plane of the stage. The pipette is first moved a few micrometers above the cell and then pushed on it, which makes the approaching more reliable. The pipette is moved closer to the target in small steps per second. The impedance of the tip is continuously monitored during the movement. An early increase in resistance denotes the presence of an obstacle in front of the pipette, e.g. a blood vessel or another cell. If an obstacle is hit, an avoidance algorithm takes over control: the pipette is pulled back, slightly moved laterally and when the obstacle is passed the pipette is oriented back to the initial trajectory towards the target. If multiple obstacles are found, the pipette is moved laterally in a spiral pattern after each hit. Meanwhile, the described 3D tracking algorithm compensates for the possible displacement of the target cell in the trajectory. When the pipette tip reaches the target position above the cell the pressure is decreased to a low positive value. Then the pipette is lowered in the Z direction and the resistance of the tip is monitored by injecting -10 pA current for 5 ms periodically. If the impedance increases more than a predefined value (0.7-1.2 MΩ) the cell membrane penetration protocol is initiated. The cell-attached configuration

is set up by the immediate cease of pressure. Small negative pressure is applied to acquire tight sealing of the cell membrane into the glass. If seal resistance reaches 1 GΩ ("gigaseal") on -60 mV holding potential then vacuum pulses of increasing length are applied to break-in the membrane and reach the whole-cell configuration. A representative patch clamp process is demonstrated in Fig. 8 including the detected cells in an image stack, the trajectory of the pipette, and the measured pressure and resistance values. Information about the process is always up to date in the GUI windows. Every parameter that has effect on the process can be set by the user.

We demonstrated the power of this system and its capability of measuring a large set of rodent and human neurons in the brain cortex. The measured records are compatible with and were inserted into the database of the Allen Institute for Brain Science. The nuclei or the cytoplasm of some measured cells were extracted after the recording and characterized molecularly. Single-cell RNA sequencing confirmed unique transcriptomal properties of cell types. The system is easily portable to any existing microscope setups. Our system is the first that can operate on unstained tissues using deep learning that reaches and even outperforms the cell detection accuracy of human experts, and the number of recordings can be multiplied while preserving high-quality measurements. Although it does not completely substitute human experts, it speeds up the recording process, shortens the learning curve of electrophysiologists and one operator can control multiple devices at the same time. Our future plans include the extension to multiple pipettes to study the connection between pairs, triplets or higher number of neurons at a time.

The author's main contributions to this work are the following:

- Development of algorithms.
- Development of the control software.
- Performing electrophysiological measurements.

# Bibliography


[1] K. Koos, J. Molnár, and P. Horvath, "DIC microscopy image reconstruction using a novel variational framework," in *2015 International Conference on Digital Image Computing: Techniques and Applications (DICTA)*, pp. 1–7, IEEE, 2015.

[2] K. Koos, J. Molnár, L. Kelemen, G. Tamás, and P. Horvath, "DIC image reconstruction using an energy minimization framework to visualize optical path length distribution," *Scientific reports*, vol. 6, p. 30420, 2016.

[3] K. Koos, B. Peksel, and L. Kelemen, "Phase measurement using DIC microscopy," *Acta Cybernetica*, vol. 23, no. 2, pp. 629–643, 2017.

[4] K. Koos, J. Molnár, and P. Horvath, "Pipette Hunter: Patch-clamp pipette detection," in *Scandinavian Conference on Image Analysis*, pp. 172–183, Springer, 2017.

[5] K. Koos, G. Oláh, T. Balassa, N. Mihut, M. Rózsa, A. Ozsvár, E. Tasnádi, J. Molnár, P. Barzó, G. Molnár, G. Tamás, and P. Horvath, "Deep learning driven label-free image guided automatic patch clamp system for human and rodent in vitro slice physiology," *Manuscript*.

[6] F. Wandrey, C. Montellese, K. Koos, L. Badertscher, L. Bammert, A. G. Cook, I. Zemp, P. Horvath, and U. Kutay, "The NF45/NF90 heterodimer contributes to the biogenesis of 60S ribosomal subunits and influences nucleolar morphology," *Molecular and cellular biology*, vol. 35, no. 20, pp. 3491–3503, 2015.

[7] K. Smith, F. Piccinini, T. Balassa, K. Koos, T. Danka, H. Azizpour, and P. Horvath, "Phenotypic image analysis software tools for exploring and understanding big image data from cell-based assays," *Cell systems*, vol. 6, no. 6, pp. 636–653, 2018.